


Article

Broad Tunable and High-Purity Photonic Microwave Generation Based on an Optically Pumped QD Spin-VCSEL with Optical Feedback

Zhenye Shen ¹, Yu Huang ¹, Xin Zhu ^{1,2}, Pei Zhou ^{1,3,*} , Penghua Mu ⁴ and Nianqiang Li ^{1,3,5,*}

¹ School of Optoelectronic Science and Engineering, Soochow University, Suzhou 215006, China

² Matrix Opto. Co., Ltd., Zhangjiagang 215614, China

³ Key Lab of Advanced Optical Manufacturing Technologies of Jiangsu Province & Key Lab of Modern Optical Technologies of Education Ministry of China, Soochow University, Suzhou 215006, China

⁴ Institute of Science and Technology for Opto-Electronic Information, Yantai University, Yantai 264005, China

⁵ State Key Laboratory of Millimeter Waves, Southeast University, Nanjing 210096, China

* Correspondence: peizhou@suda.edu.cn (P.Z.); nli@suda.edu.cn (N.L.)

Abstract: Spin-polarized vertical-cavity surface-emitting lasers (spin-VCSELs) with birefringence-induced polarization oscillations have been proposed to generate desired photonic microwave signals. Here, we numerically investigate the generation of photonic microwave signals in an optically pumped quantum dot (QD) spin-VCSEL. First, the influence of intrinsic key parameters on period-one (P1) oscillations and microwave properties is discussed. Second, the difference between microwave generation based on the quantum well (QW) and QD spin-VCSELs is analyzed by controlling the carrier capture rate that is described in the spin-flip model. The QD spin-VCSEL shows superior microwave quality in the low-frequency range (e.g., 10 GHz~20 GHz) compared with the QW spin-VCSEL. Finally, to boost the performance of the generated photonic microwave signal, optical feedback is introduced. The results show that dual-loop feedback can simultaneously narrow the microwave linewidth and suppress the side modes that are derived from the external cavity mode.

Keywords: microwave photonics; vertical-cavity surface-emitting lasers; period-one oscillation; quantum dot; spin-VCSELs; optical feedback



Citation: Shen, Z.; Huang, Y.; Zhu, X.; Zhou, P.; Mu, P.; Li, N. Broad Tunable and High-Purity Photonic Microwave Generation Based on an Optically Pumped QD Spin-VCSEL with Optical Feedback. *Photonics* **2023**, *10*, 326. <https://doi.org/10.3390/photonics10030326>

Received: 16 February 2023

Revised: 12 March 2023

Accepted: 16 March 2023

Published: 18 March 2023



Copyright: © 2023 by the authors. Licensee MDPI, Basel, Switzerland. This article is an open access article distributed under the terms and conditions of the Creative Commons Attribution (CC BY) license (<https://creativecommons.org/licenses/by/4.0/>).

1. Introduction

Photonic microwave signal generation techniques play a pivotal role in microwave photonic technologies [1–4] and usually include direct modulation [5,6], external modulation [7,8], optoelectronic oscillators (OEOs) [9–11], optical heterodyning of dual-wavelength lasers [12], and period-one (P1) dynamics [13–22]. Since the above-mentioned methods circumvent some confines of electronic approaches, they have the potential to shine in fields such as radio-over-fiber (ROF) systems [14], broadband wireless links [23,24], satellite communications, and radar [2,19,25]. To further curtail the use of the electronic facility, photonic microwave signal generation based on the P1 oscillation has attracted the bulk of concentrations in recent years, especially through the merits of all-optical component configurations, the nearly single sideband (SSB) spectrum, and wide tunability of frequencies. It is known that the optical injection in semiconductor lasers is the prospective approach to yield the P1 oscillation. In general, the P1 oscillation is generated from a stable laser driven by external perturbations, where the relaxation oscillation (RO) becomes undamped via a Hopf bifurcation. The photonic microwave signals originate from the beating between the redshifted cavity frequency component and another dominant frequency component regenerated from the optical injection. The corresponding frequencies, which far exceed the RO frequency of the laser, could be tuned by adjusting the frequency detuning between the master laser and slave laser.

The aforementioned photonic microwave generation based on P1 oscillations has been employed and investigated in several types of semiconductor lasers, including distributed feedback (DFB) lasers, quantum dot (QD) lasers, and vertical-cavity surface-emitting-lasers (VCSELs) [13,18,26–30]. Among these, spin-polarized VCSELs (spin-VCSELs) usually own lower thresholds, the capacity for spin-control of the output polarization, and faster dynamics compared to their conventional counterparts [31,32]. For spin-VCSELs, it is feasible to manipulate the output optical polarization and obtain abundant nonlinear dynamics with the contribution of coupling between the carrier spin and photons by the approach of the injection of spin-polarized electrons via magnetic contact and circularly polarized light using optical pumping. In addition, with no need for additional external perturbations, periodical polarization oscillations can be produced in a free-running optically pumped spin-VCSEL, in which the corresponding frequency stems from the cavity birefringence. Remarkably, Gerhardt et al. experimentally confirmed the birefringence splitting over 250 GHz in the VCSEL's structure through manipulating the mechanically induced strain [33]. Motivated by these appealing performances, the optically pumped quantum well (QW) spin-VCSEL has been experimentally and numerically investigated to generate the photonic microwave signal in our previous work [34,35]. Furthermore, Alharthi has also analyzed the microwave photonic signal generation in optically-injected QW spin-VCSELs theoretically [36]. Therefore, relying on highly tunable frequency oscillation and a simple structure, spin-VCSELs have come to prominence in the field of photonic microwave generation.

Besides, owing to the advances in material techniques and the preparation process, the exhilarating progress of the optically pumped QD vertical cavity devices has been further reported [37,38]. The QD spin-VCSEL owns the three-dimension confinement of carriers in its nano-structure and could be manipulated for polarized dynamics with additional degrees of freedom [39,40]. By theoretically investigating the model for the QD spin-VCSEL in the renowned spin-flip model (SFM) equations via direct simulation and the continuation package, AUTO, the instability/stability analysis and systematic bifurcation study have been unveiled elaborately in previous works [39,41]. In particular, P1 polarization oscillation induced by birefringence splitting demanded in photonic microwave generation has also been realized in QD spin-VCSELs, which can facilitate better performance with the exhibition of low threshold, less temperature sensitivity, and design flexibility [42]. In 2016, Wang et al. showed the photonic microwave generation based on the QD laser subject to optical injection [27]. Additionally, Chen et al. reported better SSB performance under optically injected QD lasers in the optical spectrum compared with QW lasers [43]. Jiang et al. also acquired the photonic microwave signals by sole excited-state emitting QD lasers [44]. However, up to now, the scenario of QD spin-VCSELs in the field of microwave generation is still obscure, which desires further devotion to probe into their potential and the disparity of the quality of microwave signals generated in QW and QD spin-VCSELs.

In this paper, we propose and demonstrate a novel photonic microwave generation scheme based on the P1 oscillation of optically pumped QD spin-VCSELs. For the P1 oscillation, we examine the role of some intrinsic key parameters on its scope of change, as well as the corresponding signal frequency and power. According to the transition revealed between the QW and QD spin-VCSELs [39,41], we carry out the inspection on the distinction of microwave quality under two conditions of spin-VCSELs when considering the variation of the carrier capture rate alone. Furthermore, to mitigate the negative influence of the linewidth expansion and phase noise occasioned by the intrinsic spontaneous emission noise in spin-VCSELs, optical feedback is harnessed into our scheme. After the introduction, the simulation model is elaborated in Section 2. The effect of key parameters on the P1 region, as well as the improvement in the quality of microwave signals through optical feedback, are investigated in Section 3. Finally, the conclusion is presented in Section 4.

2. Theoretical Model

Based on the expanding SFM, the rate equations for the QD spin-VCSEL with optical feedback can be modeled as follows [39,41]:

$$\frac{dE_{\pm}}{dt} = \kappa(n_{QD}^{\pm} - 1)(1 + i\alpha)E_{\pm} - (\gamma_a + i\gamma_p)E_{\mp} + k_{f1}E_{\pm}(t - \tau_1)e^{-i2\pi f_0\tau_1} + k_{f2}E_{\pm}(t - \tau_2)e^{-i2\pi f_0\tau_2} + F_{\pm}, \quad (1)$$

$$\frac{dn_{WL}^{\pm}}{dt} = \eta_{\pm}\gamma_n + h\frac{\gamma_n}{2} - \gamma_0 n_{WL}^{\pm} \left[\frac{h - n_{QD}^{\pm}}{2h} \right] \mp \gamma_j(n_{WL}^{+} - n_{WL}^{-}), \quad (2)$$

$$\frac{dn_{QD}^{\pm}}{dt} = \gamma_0 \frac{n_{WL}^{\pm}}{h} (h - n_{QD}^{\pm}) - \gamma_n (h + n_{QD}^{\pm}) \mp \gamma_j (n_{QD}^{+} - n_{QD}^{-}) - 2\gamma_n n_{QD}^{\pm} |E_{\pm}|^2, \quad (3)$$

where E_{+} and E_{-} denote the complex electric field amplitudes for the right and left circular polarizations (RCP and LCP), and the normalized conduction band carrier concentrations (n) with the subscripts WL and QD represent wetting layer and the quantum dot ground state, with the superscripts $+$ ($-$) representing the spin-down (spin-up). The parameters used are defined as follows: κ is the photon decay rate, α is the linewidth enhancement factor, γ_a is the dichroism (gain anisotropy), γ_p is the linear birefringence rate, γ_n is the recombination rate of carriers from the QD ground state, γ_0 is the carrier capture rate from the WL to the QD, γ_j is the spin relaxation rate, h is the normalized gain coefficient, and η_{+} (η_{-}) is the right (left) circularly polarized component of the pump, which describes the total normalized pump intensity, η ($=\eta_{+} + \eta_{-}$), and polarization ellipticity, P ($=(\eta_{+} - \eta_{-})/(\eta_{+} + \eta_{-})$). The feedback parameters include the feedback strength, k_f , and the feedback delay time, τ , of which subscripts 1 and 2 represent two different feedback loops. The center frequency of the free-running QD spin-VCSEL is denoted by f_0 . The last term, $F_{\pm} = \sqrt{\beta_{sp}\gamma_n n_{QD}^{\pm}} \xi^{\pm}$, represents the spontaneous emission noise term [45], in which β_{sp} is the spontaneous emission rate, and ξ^{\pm} is the complex Gaussian white noise of the unitary variance and zero mean value.

The differential equations given by Equations (1)–(3) are solved via the fourth-order Runge-Kutta method in MATLAB. Owing to the fact that the dynamics of VCSELs can be successfully mimicked and the SFM has been widely used, the values of parameters in [41,46], especially the inherent parameters, are considered in our manuscript. Here, a basic set of parameters are used if not mentioned otherwise: $\kappa = 250 \text{ ns}^{-1}$, $\alpha = 3$, $h = 1.1995$, $\eta = 4$, $P = 0.7$, $\gamma_a = 0 \text{ ns}^{-1}$, $\gamma_n = 1 \text{ ns}^{-1}$, $\gamma_0 = 400 \text{ ns}^{-1}$, $\gamma_j = 10 \text{ ns}^{-1}$, $\gamma_p = 30\pi \text{ ns}^{-1}$, $f_0 = 1550 \text{ nm}$, and $\beta_{sp} = 6.5 \times 10^{-3}$. The optical spectrum and the radio-frequency (RF) spectrum are calculated by the fast Fourier transform based on E_{\pm} and $|E_{\pm}|^2$, respectively, where a time step of 1 ps and a time duration of 10 μs are utilized. Additionally, a time duration of 0.2 ms, representing the spectral resolution of 5 kHz, is used to analyze the linewidth of microwave and millimeter wave signals by smoothing and fitting the spectrum.

3. Results and Discussion

3.1. P1 Oscillation in a Solitary Optically Pumped QD Spin-VCSEL

To begin with, the P1 oscillation in a solitary optically pumped QD spin-VCSEL is considered. The optical spectra and the RF spectra are shown in Figures 1a,b, respectively. The related parameters are described in the caption of Figure 1, where the optical spectra are offset to the optical frequency of the free-running QD spin-VCSEL. It is worth noting that only the RCP components are considered in our study because of the similarity of output results from the RCP and LCP components. As we can see in Figure 1a, the interval frequency between two dominant orthogonally polarized mode components in the optical spectrum corresponds with the frequency of generated microwave signals after beating in the photodetector, as presented in the RF spectrum of Figure 1b, which is roughly close to γ_p/π [32]. Unlike other kinds of semiconductor lasers invoking P1 dynamics by undamping the RO at the Hopf bifurcation point, the induced oscillation frequency from the spin-VCSEL originates from the birefringence split, vastly exceeding the RO frequency given by $f_{RO} = [2\kappa\gamma_n(\eta - 1)]^{1/2}/(2\pi)$ [47]. In this work, the RO frequency is calculated to be 6.16 GHz for $\eta = 4$. When the birefringence is set as $30\pi \text{ ns}^{-1}$, the

fundamental microwave frequency obtained from the beating of two dominant mode components is 32.43 GHz, where the spectrum linewidth obviously broadens to 1.52 MHz, as shown in Figure 1(b1), owing to the intrinsic spontaneous emission noise of semiconductor lasers. When the birefringence, γ_p , is increased to $60\pi \text{ ns}^{-1}$, the microwave frequency of 61.52 GHz with a linewidth of 2.14 MHz is shown, as seen in Figure 1(b2). By further enhancing the birefringence, γ_p , to $90\pi \text{ ns}^{-1}$, the fundamental frequency reaches 90.86 GHz with a corresponding linewidth of 2.20 MHz, as shown in Figure 1(b3). Obviously, the practicable result is tuning the oscillation frequency with the birefringence, which is governable in the experiment. Moreover, the spectrum broadening needs to be further suppressed for preferable microwave quality, which will be discussed in a later section.

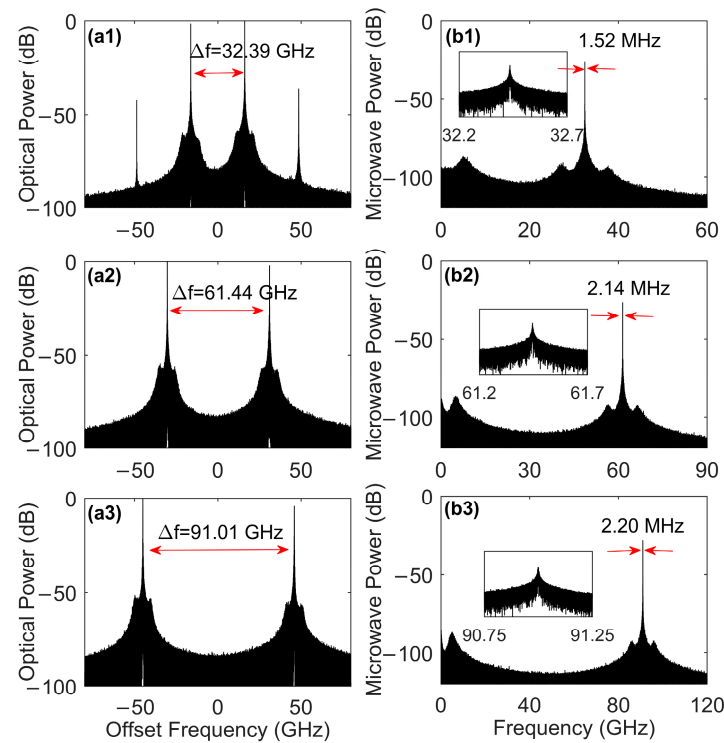


Figure 1. (a1–a3) Optical spectra and (b1–b3) RF spectra of the solitary optically pumped QD spin-VCSEL. (a1,b1) $\gamma_p = 30\pi \text{ ns}^{-1}$, (a2,b2) $\gamma_p = 60\pi \text{ ns}^{-1}$, and (a3,b3) $\gamma_p = 90\pi \text{ ns}^{-1}$. Other parameters are set as $\gamma_j = 10 \text{ ns}^{-1}$, $\gamma_a = 0 \text{ ns}^{-1}$, $\gamma_n = 1 \text{ ns}^{-1}$, $\gamma_o = 400 \text{ ns}^{-1}$, $\kappa = 250 \text{ ns}^{-1}$, $\alpha = 3$, $h = 1.1995$, $\eta = 4$, and $p = 0.7$.

3.2. The Effect of Intrinsic Parameters on the Microwave Characteristics

For a better idea of the effects of the two key parameters on microwave signals, herein we investigate the frequency and power of microwaves for several values of parameters, i.e., the linewidth enhancement factor, α , and normalized gain coefficient, h . In reality, the impact of some intrinsic parameters on VCSEL dynamics has been exploratively revealed [41]. In this section, we mainly focus on the microwave frequency and power in the plane of the spin relaxation rate, γ_j , and birefringence rate, γ_p . Specifically, by numerically calculating the extrema (maxima and minima) of the intensity time traces, different dynamics can be identified as continuous-wave (CW), P1, period-two (P2), and complex dynamics. In order to minutely explore the P1 oscillation, the CW and other complex dynamics are marked in white, while the colorful regions, corresponding to different microwave powers, represent the P1 oscillation area. In this study, microwave power is defined as the peak power of the fundamental frequency in the RF spectrum. As shown in Figure 2(a1–a3), the bifurcation maps are obtained for $h = 1.1995$, where α is increased from 2 to 4. One can clearly see that the P1 dynamic regime is largely expanded with the increase of α . At the same time, the white oval region on the bottom of the graphs is also magnified, which may compromise

the generation of low-frequency microwaves. For a larger value of $h = 2$ in Figure 2b, the enlarged P1 dynamic area still shows a trend of expansion in size when the linewidth enhancement factor, α , is increased. Compared with the left column, this tendency becomes more evident, and the whole area of the P1 regime shifts toward the right of the map, i.e., the direction of the high spin relaxation rate. Next, we focus on the characteristics of the microwave signals in the (γ_j, γ_p) plane. From Figure 2, the microwave signal frequencies are enhanced almost synchronously with the increment of the birefringence. In terms of microwave power, the distribution of low power is mainly concentrated on the outline area of the P1 oscillation region, i.e., the vicinity of two Hopf bifurcation branches. In other words, the power of the microwave signals is easily kept at high values on the map, which is critical in practice.

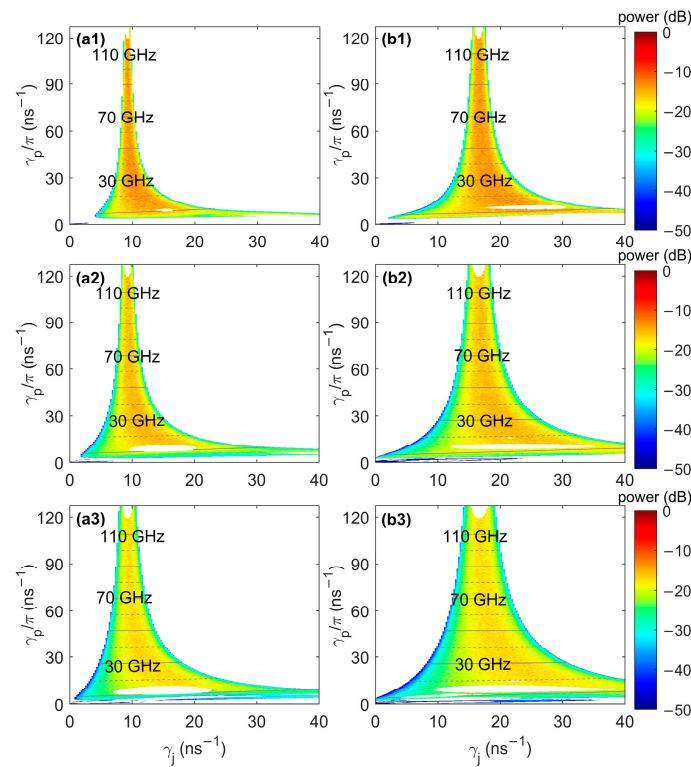


Figure 2. Calculated color maps for the microwave power in the (γ_j, γ_p) plane. (a1,b1) $\alpha = 2$, (a2,b2) $\alpha = 3$, (a3,b3) $\alpha = 4$, where $h = 1.1995$ in the column (a), and $h = 2$ in the column (b). The color bars on the right represent microwave power.

Next, we consider the impact of the carrier capture rate on the characteristics of microwave signals. Figure 3a displays the color map in the (γ_o, γ_j) plane, where γ_p increases from $10\pi \text{ ns}^{-1}$ to $30\pi \text{ ns}^{-1}$. One can clearly see that the P1 dynamics regime shrinks slightly with the variation of γ_j , while the main distribution of the P1 region expands toward the right of the map, i.e., the direction of the high carrier capture rate. Likewise, relatively large power is obtained in most regions, and the low power majorly concentrates near the underneath boundary of the P1 oscillation. Then, we analyze the influence of the carrier capture rate, γ_o , and the birefringence, γ_p , in Figure 3b, where γ_j augments from 10 ns^{-1} to 20 ns^{-1} . The P1 oscillation greatly dilates in size and moves to larger values of γ_o with the increasing of the spin relaxation rate, γ_j . Precisely speaking, the relatively high-frequency region is shifted to the direction of high γ_o . In addition, the relatively large microwave power can be sustained in Figure 3(b3) when γ_j is set to 20 ns^{-1} . However, the results in Figure 3(b1,b2) suggest that the higher microwave power is majorly located in the left region of the map, where a low γ_o is principally selected in the QD spin-VCSEL.

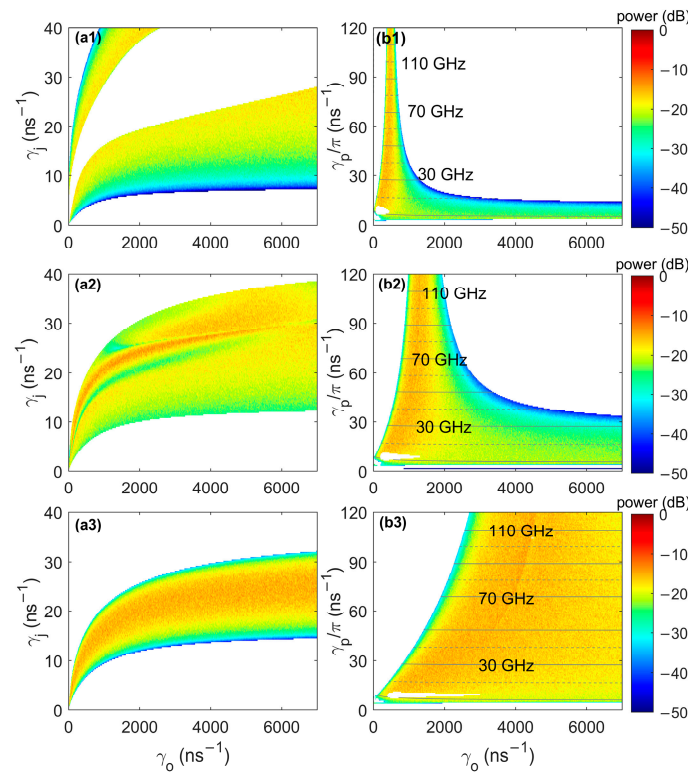


Figure 3. Calculated color maps for the microwave power in the (γ_o, γ_j) plane (left column) and (γ_o, γ_p) plane (right column). (a1) $\gamma_p = 10\pi \text{ ns}^{-1}$, (a2) $\gamma_p = 20\pi \text{ ns}^{-1}$, and (a3) $\gamma_p = 30\pi \text{ ns}^{-1}$. (b1) $\gamma_j = 10 \text{ ns}^{-1}$, (b2) $\gamma_j = 15 \text{ ns}^{-1}$, and (b3) $\gamma_j = 20 \text{ ns}^{-1}$. The colored regions indicate the P1 dynamics, while the CW and other complex dynamics, including chaos, are marked as white. The color bars on the right represent microwave power.

It is known that the transition from QD to QW could be realized in the proposed model described by Equations (1)–(3) if we consider that the capture of carriers from the WL to GS increases instantaneously, e.g., $\gamma_o = 7000 \text{ ns}^{-1}$. The similarities and differences in the dynamics between typical QD and QW spin-VCSELs have been explored in our previous work [41]. In this section, we assume that the QD spin-VCSEL with the value of $\gamma_o = 7000 \text{ ns}^{-1}$ represents the case of the QW spin-VCSEL and compare the performance of the generated microwave signals in QW and QD spin-VCSELs. Figure 4 shows the optical spectra and RF spectra of a QD spin-VCSEL when the value of γ_o is 400 ns^{-1} and 7000 ns^{-1} . The birefringence of $10\pi \text{ ns}^{-1}$ is selected for a better comparison. Compared with Figure 4(a1), the optical spectrum in Figure 4(a2) shows the two dominant mode components with lower power, which results in lower power of the fundamental microwave frequency (see Figure 4b). The microwave linewidth is distinctly elevated from 1.48 MHz to 3.79 MHz with the growth of γ_o , which means that the quality of signals is degraded due to the transition from the QD to QW. Moreover, there is a slight increase in the corresponding fundamental frequency of microwaves from 13.53 GHz to 14.3 GHz.

In order to gain more insight into the characteristics of microwave signals as the capture rate γ_o varies, Figure 5 presents the results for the microwave frequency, power, linewidth, and phase noise. The results for the spin relaxation rate of $\gamma_j = 10 \text{ ns}^{-1}$ and the birefringence of $\gamma_p = 10\pi \text{ ns}^{-1}$ are represented by circles, while those for $\gamma_j = 15 \text{ ns}^{-1}$ and $\gamma_p = 30\pi \text{ ns}^{-1}$ are symbolized by triangles. Both cases, represented by circles and triangles in Figure 5a, show a stunning rise in their estimated linewidth with the increase of γ_o . In the meantime, a similarly destructive phenomenon can be found in the observation of the phase noise variance in Figure 5b. In addition, the decline of microwave power agrees well with that shown in Figure 3. The influence of γ_o on the microwave frequency is

also recorded in the insets (c1,c2), where the results show that the frequency rises steadily within only about 1 GHz and 0.4 GHz, respectively, in both cases. All of these tendencies vividly reveal that a high γ_o is not advantageous for generating high-quality microwave signals under the conditions shown above.

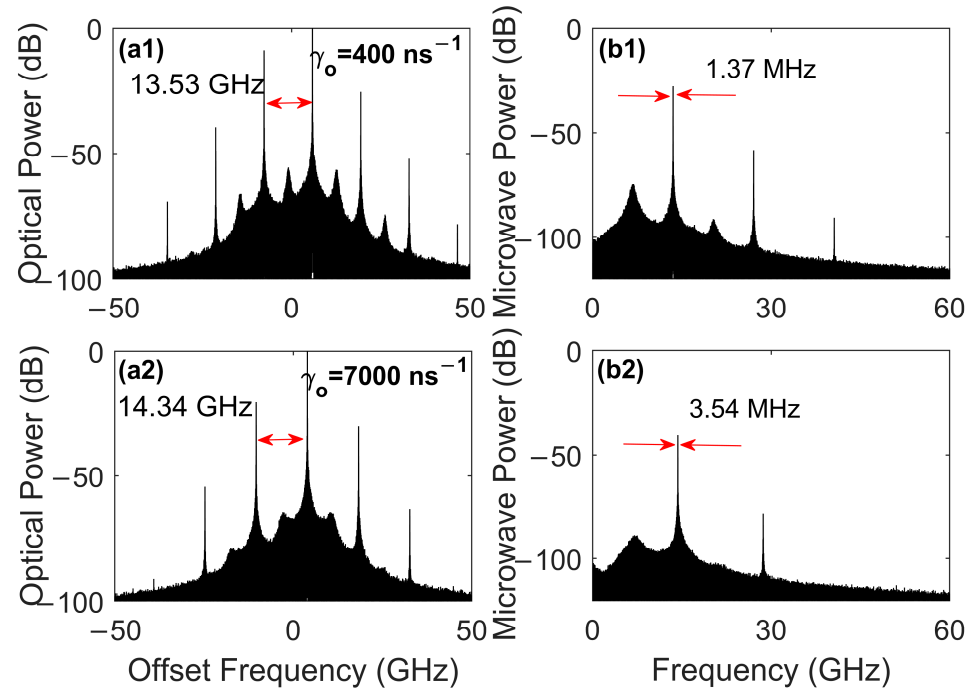


Figure 4. (a1,a2) Optical spectra and (b1,b2) RF spectra of the solitary optically pumped QD spin-VCSEL with (a1,b1) $\gamma_o = 400 \text{ ns}^{-1}$ and (a2,b2) $\gamma_o = 7000 \text{ ns}^{-1}$. The spin relaxation rate is $\gamma_j = 10 \text{ ns}^{-1}$, and other parameters are the same as those in Figure 1.

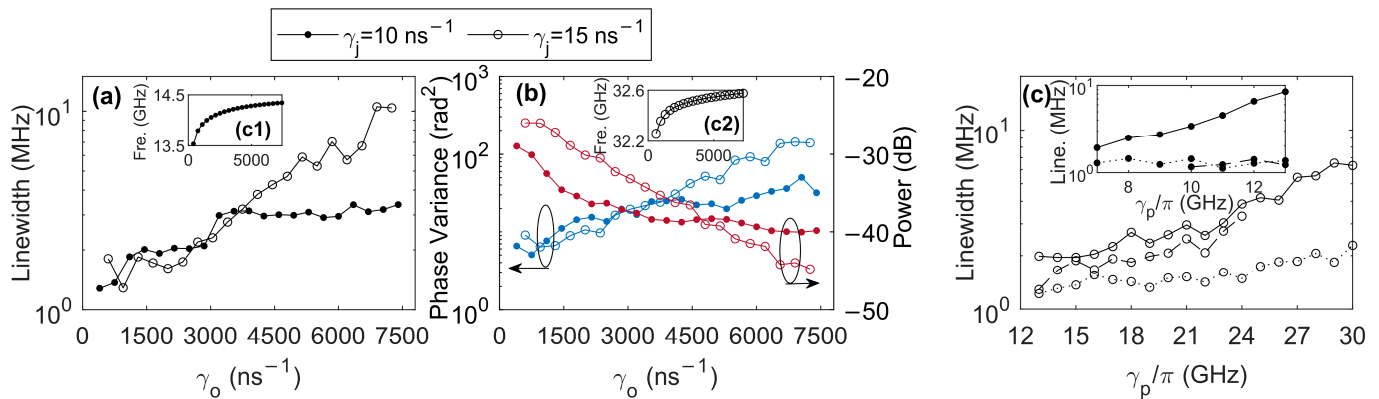


Figure 5. (a) Microwave linewidth, (b) phase noise variance (blue curve), power (crimson curve), and inset (c1,c2) microwave frequency of the solitary optically pumped QD spin-VCSEL versus the carrier capture rate, γ_o . The solid dots indicate $\gamma_j = 10 \text{ ns}^{-1}$ and the birefringence, $\gamma_p = 10\pi \text{ ns}^{-1}$, and the empty circles represent $\gamma_j = 15 \text{ ns}^{-1}$ and $\gamma_p = 30\pi \text{ ns}^{-1}$. (c) Microwave linewidth at $\gamma_o = 400 \text{ ns}^{-1}$ (dashed line), $\gamma_o = 600 \text{ ns}^{-1}$ (dotted line) and $\gamma_o = 7000 \text{ ns}^{-1}$ (solid line).

Similarly, on account of the transition from the QD spin-VCSEL to the QW case when the capture of the carriers, γ_o , is instantaneous, Figure 5c shows the linewidth of the microwave signals based on the QD case ($\gamma_o = 400 \text{ ns}^{-1}$ and 600 ns^{-1}) and the QW case ($\gamma_o = 7000 \text{ ns}^{-1}$) at various frequencies for $\gamma_j = 10 \text{ ns}^{-1}$ and 15 ns^{-1} . It should be mentioned that partial results for $\gamma_o = 400 \text{ ns}^{-1}$ are shown, as seen in Figure 5c, since in the rest part of the spin-VCSEL exhibits complicated dynamics rather than P1 oscillations. The results suggest that the broader linewidth can be encountered for the QW spin-VCSEL, and here

we focus on the frequency (γ_p/π) between 10 GHz to 20 GHz, where both QW and QD spin-VCSELs operate in P1 dynamics and thus allows for a fair comparison. Despite the γ_o not being an experimentally accessible parameter, its evident impact on the characteristics of microwave signals may set the scene for the contrast of microwave quality generated by QW and QD spin-VCSELs, which is eager to be further verified and disclosed in practical applications.

3.3. P1 Oscillation in the Optically Pumped QD Spin-VCSEL with Optical Feedback

In this section, polarization-preserved optical feedback is adopted to reduce the broadening spectrum linewidth due to the intrinsic spontaneous emission noise in the QD spin-VCSEL for higher microwave signal purity. The results for optical spectra and RF spectra are shown in Figure 6, where both single-loop feedback and dual-loop feedback are included. As shown in Figure 6(b1), the microwave linewidth is minimized from 1.52 MHz (without optical feedback) to 15 kHz through single-loop feedback ($k_f = 2.5 \text{ ns}^{-1}$, $\tau = 4 \text{ ns}$) in the RF spectrum, in which the relevant parameters are the same as those in Figure 1. Attributing to the adoption of the feedback loop, many side peaks, which stand for the external cavity modes, emerge around the dominant components in Figure 6b. Correspondingly, the side peaks around the fundamental frequency are approximately separated by the multiples of the reciprocal of the feedback delay time, i.e., $1/\tau$. Compared to the peak of the central fundamental frequency, however, these side peaks are rather weak and do not affect the calculation of the spectrum linewidth. To accurately analyze the relationship between these side peaks, the side peak suppression coefficient (SPSC) is defined as the ratio between the power of the maximum side peak and the power of the fundamental frequency. The SPSC reaches 44 dB in Figure 6(b1) with single-loop feedback.

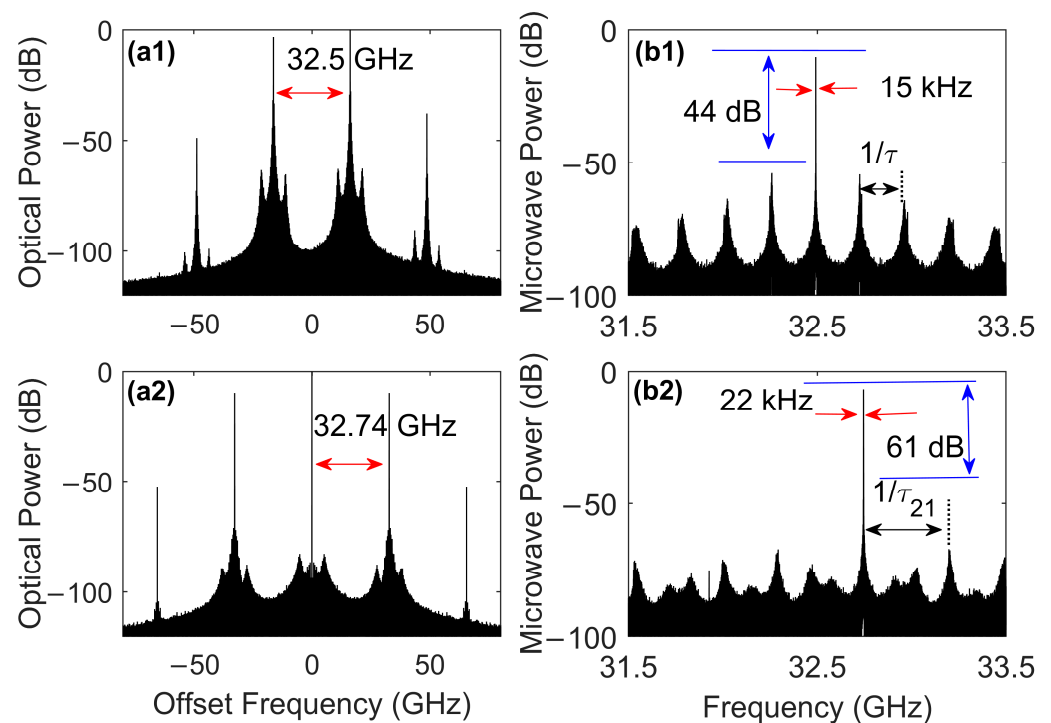


Figure 6. (a1,a2) Optical spectra and (b1,b2) RF spectra of the optically pumped QD spin-VCSEL subject to (a1,b1) single-loop feedback and (a2,b2) dual-loop feedback. The feedback strengths are fixed at $k_f = 2.5 \text{ ns}^{-1}$ and $(k_{f1}, k_{f2}) = (1.5 \text{ ns}^{-1}, 1.5 \text{ ns}^{-1})$. The feedback delay times are set as $\tau = 4 \text{ ns}$ and $(\tau_1, \tau_2) = (4 \text{ ns}, 6.5 \text{ ns})$ in (b). Other parameters are the same as those in Figure 1 (a1,b1).

To further improve the quality of microwave signals, dual-loop optical feedback is employed, where the difference of two delay times is $\tau_{21} = \tau_2 - \tau_1$, and the total of

two feedback strengths is equal to that of the single-loop feedback, i.e., $k_f = k_{f1} + k_{f2}$. In Figure 6(b2), one can see that the residual side peaks are separated by multiples of the reciprocal of the averaged delay time, i.e., $1/\tau_{21}$. Furthermore, the linewidth is slightly increased to 22 kHz, and the side peaks are visibly restrained, while the SPSC is improved to about 61 dB due to the competition of external cavity modes attracted from dual-loop feedback with dissimilar delay times.

To investigate the microwave quality versus feedback parameters, the one-parameter bifurcation diagram, as a function of the feedback strength, is used to describe the stability of the P1 dynamics state. Figure 7 displays the results for both single-loop and dual-loop feedback cases. The feedback delay time is set to $\tau = 4$ ns in the single-loop feedback and those are set to $\tau_1 = 4$ ns and $\tau_2 = 6.5$ ns in the dual-loop feedback where the essential difference between the two delay times is to activate the Vernier effect. The other parameters are set the same as those in Figure 1. As can be seen from both subfigures, the P1 dynamics remain for low values of the feedback strength. When the feedback strength exceeds a certain value, e.g., $k_f = \sim 3$ ns⁻¹ (see Figure 7a), the adequately strong strength drives the VCSEL into unstable P1 dynamics and other complicated nonlinear dynamics, such as period-doubling and chaos. By contrast, despite the exhibition of unstable P1 oscillation and complex dynamics in the strong feedback strength area, P1 oscillations with dual-loop feedback can be maintained over a large scope, e.g., the range between $k_f = 3$ ns⁻¹ and $k_f = 4$ ns⁻¹, which sets the stage for its elegant enhancement of the microwave quality in the following description.

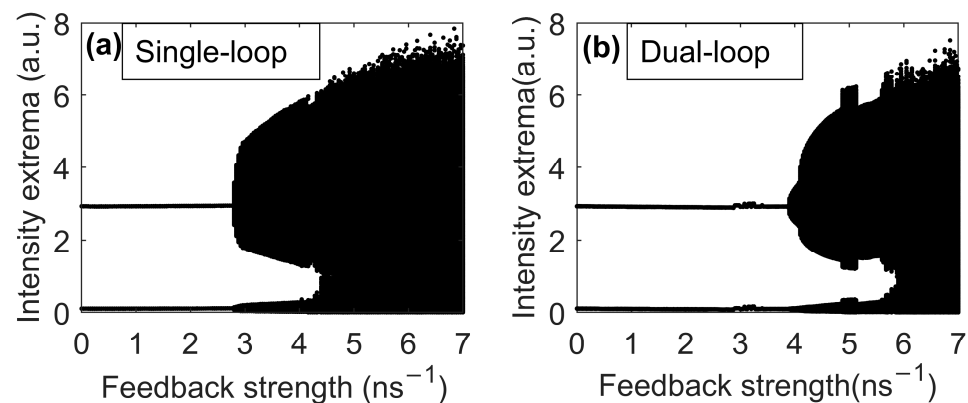


Figure 7. The bifurcation of an optically pumped QD spin-VCSEL subject to (a) single-loop feedback and (b) dual-loop feedback. The delay times are fixed at $\tau = 4$ ns for single-loop feedback and $(\tau_1, \tau_2) = (4$ ns, 6.5 ns) for dual-loop feedback.

Figure 8 presents the properties of the microwave spectral purity, including the 3-dB linewidth and phase noise and their dependence on key feedback parameters under different optical feedback conditions. The feedback delay time is kept at the same value as in Figure 7, and the two feedback strengths are set to be equivalent in dual-loop feedback. From Figure 8(a1), we can see that the two linewidth lines through single-loop feedback (depicted as the black dots) and dual-loop feedback (shown as the red dots) experience a commensurate decline first and fluctuate down to the flatter areas. The ascending trends are then observed when the feedback strength exceeds the minimum point at near $k_f = 3$ ns⁻¹ (in the single-loop feedback) and $k_f = 4$ ns⁻¹ (in the dual-loop feedback). This can be attributed to the evolution of the unstable dynamics and complex dynamics states of the QD spin-VCSELs described in Figure 7a. It is worth mentioning that a narrower spectrum linewidth dwelling at some values of feedback strengths can be obtained in relatively smooth regions if a longer simulation time duration is undertaken, which usually corresponds to a higher resolution. With respect to the investigation of the side peaks in Figure 8(a2), similarly, the SPSC in the single-loop feedback case holds a steady trend in the weak feedback strength area and then decreases dramatically owing to the excitation of strong side peaks as the feedback strength increases. For the scenario of dual-loop feedback,

the SPSC can maintain a higher value range by suppressing the destructive side peaks until the feedback strength reaches $k_f = 4 \text{ ns}^{-1}$. To further investigate the microwave quality, the phase noise variance is evaluated by integrating the averaged single sideband power spectrum from the fundamental frequency offset of 3 MHz to 1 GHz [22]. As can be seen from Figure 8(a3), the variation tendencies of the phase noise variance are in accordance with that of the microwave linewidth in our above-mentioned discussion. In the strong feedback strength area, the phase variance is suppressed to the minimum value of 0.01 rad^2 when $k_f = 2.5 \text{ ns}^{-1}$, and the lower phase variance of 0.001 rad^2 emerges at $k_{f1} = 1.9 \text{ ns}^{-1}$ and $k_{f2} = 1.9 \text{ ns}^{-1}$, owing to the strict curb on the side peaks.

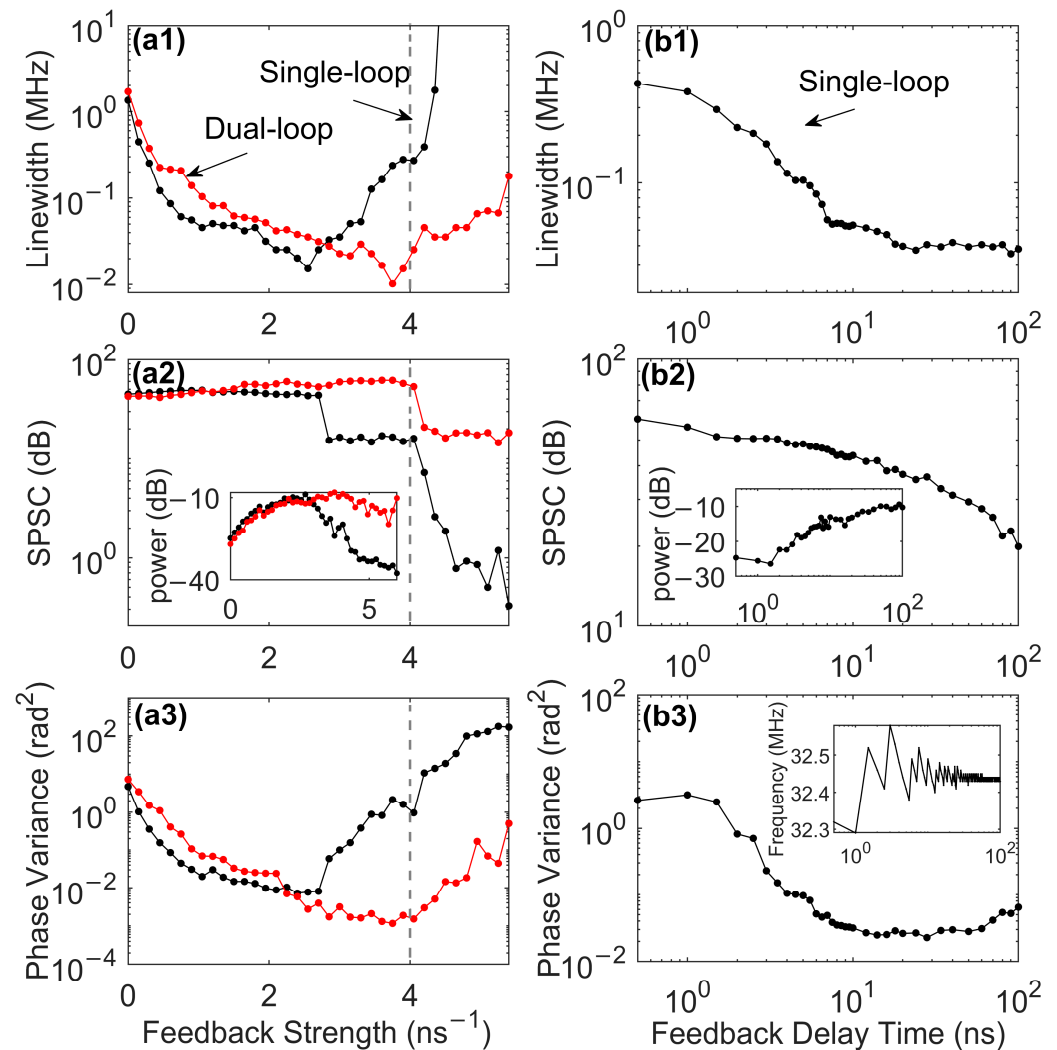


Figure 8. (a1,b1) Microwave linewidth, (a2,b2) the SPSC, and (a3,b3) phase noise variance as a function of the total feedback strength in the left column and feedback delay time in the right column. The feedback strength is set to $k_f = 3 \text{ ns}^{-1}$ when the delay time varies. The other parameters are the same as those in Figure 7.

We then evaluate the microwave quality versus the varying feedback delay time in the case of single-loop feedback. Herein, the weak feedback strength of $k_f = 0.5 \text{ ns}^{-1}$ is introduced for the intuitive exhibition of microwave characteristics. In general, when the optical feedback is introduced, the length of the feedback loop is related to the delay time, which has a great impact on the locking behavior among the P1 oscillation with the resonance modes of the feedback loops [21], which is profoundly affirmed by the hopping of the frequency in the insert of Figure 8(b3). Figure 8(b1) illustrates that a monotonous decrease appears in the linewidth of the microwave as the delay time is increased even to

large values corresponding to a long feedback loop. In other words, a longer delay time is constructive for better performance on the microwave linewidth. Nevertheless, as shown in Figure 8(b2), the continuous diminishing of the SPSC indicates the constant growth of undesired strong side peaks. Consequently, due to the disturbance of the side peaks, the improvement in the phase noise variance cannot be expected as the feedback delay time increases over certain values. For the change of the two delay times in the dual-loop feedback, the special ratio among the two feedback loop delay times should be avoided for superior side peaks' suppression in the investigation of DFB lasers and conventional VCSELs [22,30], which is also followed in this study.

By controlling the variable birefringence rate, a broadly tunable microwave frequency, from tens to a hundred gigahertz, can be attained in the optically pumped QD spin-VCSEL. In addition, improved microwave quality can be sustained by reasonably selecting the appropriate parameters through single- and dual-loop optical feedback. In Figure 9, the linewidth and phase noise variance are displayed over the varying microwave frequency in different feedback conditions, in which the different feedback parameters are chosen in those values with relatively optimized performance. Compared with the condition under no optical feedback, the decline of linewidth under the optical feedback can exceed an order of magnitude, from the magnitude of MHz to about 50 kHz and below. Furthermore, the advance of the phase noise variance may surpass two or three orders of magnitude by single- and dual-loop feedback, respectively. Under the corresponding conditions, the SPSC can sustain improved values above 40 dB and near 60 dB for single- and dual-loop feedback. As a result, high-quality microwave signals with tunable frequencies can be implemented conveniently.

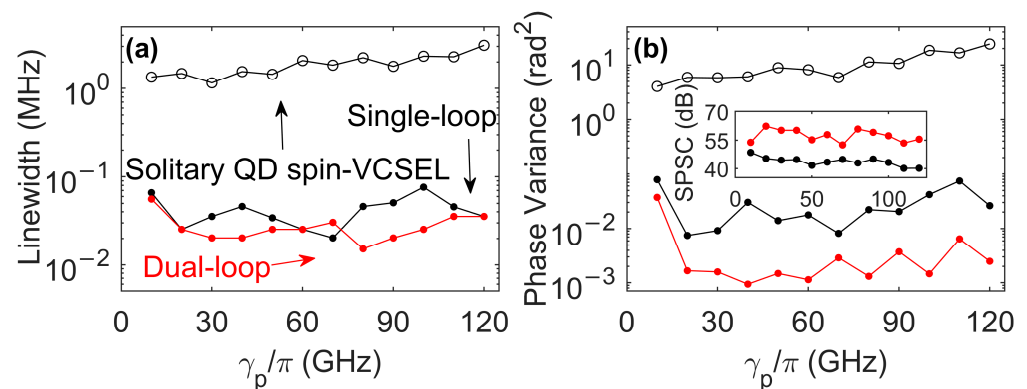


Figure 9. (a) Microwave linewidth and (b) phase noise variance as a function of P1 oscillation frequencies, where the optically pumped QD spin-VCSEL is subject to no feedback (hollow circles), single-loop feedback (black dots), and dual-loop feedback (red dots). These dots represent relatively optimized results with varying feedback parameters.

4. Conclusions

In summary, a photonic microwave signal generation system based on an optically pumped QD spin-VCSEL has been proposed and demonstrated numerically. We have investigated the effect of intrinsic key parameters on the P1 dynamics and power of microwave signals. In particular, we have compared the microwave quality between the QW and QD cases by substituting the QW spin-VCSEL with the condition of the QD spin-VCSEL when the value of the carrier capture rate is instantaneous. The relatively high-quality microwave signals in the low-frequency range can be more easily observed in the QD spin-VCSEL. Moreover, to reduce the impact of spontaneous emission noise on microwave quality, the characteristics, including the frequency, power, linewidth, phase noise, and the SPSC, of microwave signals in the case of single- and dual-loop optical feedback have been investigated. In general, we have utilized the single-loop feedback to reduce the linewidth and then further employed the dual-loop feedback to suppress the side peaks around the fundamental frequency and improve the phase noise variance. We

have discussed the influence of the feedback strength and feedback delay time on the P1 dynamics and the generated microwave signals. These results imply that the linewidth could be narrowed from the magnitude of MHz to below 50 kHz and that the improvement of the phase noise through suppressing the side peaks could reach two or three orders of magnitude by selecting appropriate feedback parameters. Compared with conventional sources, the broadband tunable microwave frequency range can be more easily achieved in the QD spin-VCSEL, with no need for an additional optical injection. Furthermore, some other characteristics, such as a smaller size, less temperature sensitivity, low-cost light sources, and accessible integration, can also be expected. We believe this scenario can offer a convenient scheme for the generation of high-quality photonic microwave signals and broaden the prospect for QD spin-VCSEL applications.

Author Contributions: Conceptualization and resources, N.L.; simulation, Z.S. and Y.H.; supervision, X.Z., P.Z. and N.L.; all authors contributed to the writing of the manuscript. P.Z. and N.L. contributed to the reviewing of the manuscript. All authors have read and agreed to the published version of the manuscript.

Funding: This study was funded by the National Natural Science Foundation of China (62004135, 62001317, 62171305, 62111530301); the Natural Science Research Project of Jiangsu Higher Education Institutions of China (20KJA416001); the Natural Science Foundation of Jiangsu Province (BK20200855); the Open Fund of the State Key Laboratory of Millimeter Waves of China (K202239).

Institutional Review Board Statement: Not applicable.

Informed Consent Statement: Not applicable.

Data Availability Statement: Data underlying the results presented in this paper are not publicly available at this time but may be obtained from the authors upon reasonable request.

Conflicts of Interest: The authors declare no conflict of interest.

References

1. Yao, J. Microwave Photonics. *J. Light. Technol.* **2009**, *27*, 314–335. [\[CrossRef\]](#)
2. Marpaung, D.; Yao, J.; Capmany, J. Integrated microwave photonics. *Nat. Photonics* **2019**, *13*, 80–90. [\[CrossRef\]](#)
3. Qi, X.-Q.; Liu, J.-M. Photonic Microwave Applications of the Dynamics of Semiconductor Lasers. *IEEE J. Sel. Top. Quantum Electron.* **2011**, *17*, 1198–1211. [\[CrossRef\]](#)
4. Chan, S.C.; Liu, J.M. Tunable Narrow-Linewidth Photonic Microwave Generation Using Semiconductor Laser Dynamics. *IEEE J. Sel. Top. Quantum Electron.* **2004**, *10*, 1025–1032. [\[CrossRef\]](#)
5. Hwang, S.K.; Liu, J.M.; White, J.K. 35-GHz intrinsic bandwidth for direct modulation in 1.3- μm semiconductor lasers subject to strong injection locking. *IEEE Photonics Technol. Lett.* **2004**, *16*, 972–974. [\[CrossRef\]](#)
6. Kjebon, O.; Schatz, R.; Lourduoss, S.; Nilsson, S.; Stalnacke, B.; Backbom, L. 30GHz direct modulation bandwidth in detuned loaded InGaAsP DBR lasers at 1.55 μm wavelength. *Electron. Lett.* **1997**, *33*, 488–489. [\[CrossRef\]](#)
7. Bortnik, B.; Hung, Y.C.; Tazawa, H.; Seo, B.J.; Luo, J.; Jen, A.K.Y.; Steier, W.H.; Fetterman, H.R. Electrooptic Polymer Ring Resonator Modulation up to 165 GHz. *IEEE J. Sel. Top. Quantum Electron.* **2007**, *13*, 104–110. [\[CrossRef\]](#)
8. Fan, L.; Xia, G.; Chen, J.; Tang, X.; Liang, Q.; Wu, Z. High-purity 60GHz band millimeter-wave generation based on optically injected semiconductor laser under subharmonic microwave modulation. *Opt. Express* **2016**, *24*, 18252–18265. [\[CrossRef\]](#)
9. Maleki, L. The optoelectronic oscillator. *Nat. Photonics* **2011**, *5*, 728–730. [\[CrossRef\]](#)
10. Yao, X.S.; Maleki, L. Multiloop optoelectronic oscillator. *IEEE J. Quantum Electron.* **2000**, *36*, 79–84. [\[CrossRef\]](#)
11. Pan, S.; Yao, J. Wideband and frequency-tunable microwave generation using an optoelectronic oscillator incorporating a Fabry-Perot laser diode with external optical injection. *Opt. Lett.* **2010**, *35*, 1911–1913. [\[CrossRef\]](#)
12. Pan, B.; Lu, D.; Sun, Y.; Yu, L.; Zhang, L.; Zhao, L. Tunable optical microwave generation using self-injection locked monolithic dual-wavelength amplified feedback laser. *Opt. Lett.* **2014**, *39*, 6395–6398. [\[CrossRef\]](#) [\[PubMed\]](#)
13. Chan, S.-C.; Hwang, S.-K.; Liu, J.-M. Period-one oscillation for photonic microwave transmission using an optically injected semiconductor laser. *Opt. Express* **2007**, *15*, 14921–14935. [\[CrossRef\]](#) [\[PubMed\]](#)
14. Cui, C.; Chan, S.-C. Performance analysis on using period-one oscillation of optically injected semiconductor lasers for radio-over-fiber uplinks. *IEEE J. Quantum Electron.* **2012**, *48*, 490–499. [\[CrossRef\]](#)
15. Lin, L.C.; Liu, S.H.; Lin, F.Y. Stability of period-one (P1) oscillations generated by semiconductor lasers subject to optical injection or optical feedback. *Opt. Express* **2017**, *25*, 25523–25532. [\[CrossRef\]](#)
16. Li, S.S.; Zou, X.; Wang, L.; Wang, A.; Pan, W.; Yan, L. Stable period-one oscillations in a semiconductor laser under optical feedback from a narrowband fiber Bragg grating. *Opt. Express* **2020**, *28*, 21286–21299. [\[CrossRef\]](#) [\[PubMed\]](#)

17. Hung, Y.-H.; Hwang, S.-K. Photonic microwave stabilization for period-one nonlinear dynamics of semiconductor lasers using optical modulation sideband injection locking. *Opt. Express* **2015**, *23*, 6520–6532. [\[CrossRef\]](#) [\[PubMed\]](#)
18. Ji, S.; Hong, Y.; Spencer, P.S.; Benedikt, J.; Davies, I. Broad tunable photonic microwave generation based on period-one dynamics of optical injection vertical-cavity surface-emitting lasers. *Opt. Express* **2017**, *25*, 19863–19871. [\[CrossRef\]](#)
19. Tseng, C.H.; Hwang, S.K. Broadband chaotic microwave generation through destabilization of period-one nonlinear dynamics in semiconductor lasers for radar applications. *Opt. Lett.* **2020**, *45*, 3777–3780. [\[CrossRef\]](#)
20. Tseng, C.-H.; Liao, B.-K.; Hwang, S.-K. All-optical, tunable, V- and W-band microwave generation using semiconductor lasers at period-one nonlinear dynamics with asymmetric mutual injection stabilization. *Opt. Lett.* **2022**, *47*, 4648–4651. [\[CrossRef\]](#)
21. Lo, K.-H.; Hwang, S.-K.; Donati, S. Numerical study of ultrashort-optical-feedback-enhanced photonic microwave generation using optically injected semiconductor lasers at period-one nonlinear dynamics. *Opt. Express* **2017**, *25*, 31595–31611. [\[CrossRef\]](#) [\[PubMed\]](#)
22. Zhuang, J.P.; Chan, S.C. Phase noise characteristics of microwave signals generated by semiconductor laser dynamics. *Opt. Express* **2015**, *23*, 2777–2797. [\[CrossRef\]](#) [\[PubMed\]](#)
23. Carpintero, G.; Balakier, K.; Yang, Z.; Guzmán, R.C.; Corradi, A.; Jimenez, A.; Kervella, G.; Fice, M.J.; Lamponi, M.; Chitoui, M.; et al. Microwave Photonic Integrated Circuits for Millimeter-Wave Wireless Communications. *J. Light. Technol.* **2014**, *32*, 3495–3501. [\[CrossRef\]](#)
24. Zeb, K.; Lu, Z.; Liu, J.; Mao, Y.; Liu, G.; Poole, P.J.; Rahim, M.; Pakulski, G.; Barrios, P.; Vachon, M.; et al. Broadband Optical Heterodyne Millimeter-Wave-over-Fiber Wireless Links Based on a Quantum Dash Dual-Wavelength DFB Laser. *J. Light. Technol.* **2022**, *40*, 3698–3708. [\[CrossRef\]](#)
25. Zhou, P.; Zhang, R.; Li, N.; Jiang, Z.; Pan, S. An RF-Source-Free Reconfigurable Microwave Photonic Radar With High-Resolution and Fast Detection Capability. *J. Light. Technol.* **2022**, *40*, 2862–2869. [\[CrossRef\]](#)
26. Lo, K.H.; Hwang, S.K.; Donati, S. Optical feedback stabilization of photonic microwave generation using period-one nonlinear dynamics of semiconductor lasers. *Opt. Express* **2014**, *22*, 18648–18661. [\[CrossRef\]](#) [\[PubMed\]](#)
27. Wang, C.; Raghunathan, R.; Schires, K.; Chan, S.-C.; Lester, L.F.; Grillot, F. Optically injected InAs/GaAs quantum dot laser for tunable photonic microwave generation. *Opt. Lett.* **2016**, *41*, 1153–1156. [\[CrossRef\]](#)
28. Hurtado, A.; Raghunathan, R.; Henning, I.D.; Adams, M.J.; Lester, L.F. Simultaneous microwave- and millimeter-Wave signal generation with a 1310-nm quantum-dot-distributed feedback laser. *IEEE J. Sel. Top. Quantum Electron.* **2015**, *21*, 568–574. [\[CrossRef\]](#)
29. Ji, S.; Xue, C.; Valle, A.; Spencer, P.S.; Li, H.; Hong, Y. Stabilization of photonic microwave generation in vertical-cavity surface-emitting lasers with optical injection and feedback. *J. Light. Technol.* **2018**, *36*, 4347–4353. [\[CrossRef\]](#)
30. Xue, C.; Chang, D.; Fan, Y.; Ji, S.; Zhang, Z.; Lin, H.; Spencer, P.S.; Hong, Y. Characteristics of microwave photonic signal generation using vertical-cavity surface-emitting lasers with optical injection and feedback. *J. Opt. Soc. Am. B* **2020**, *37*, 1394–1400. [\[CrossRef\]](#)
31. Gerhardt, N.C.; Hofmann, M.R. Spin-Controlled Vertical-Cavity Surface-Emitting Lasers. *Adv. Opt. Technol.* **2012**, *2012*, 268949. [\[CrossRef\]](#)
32. Lindemann, M.; Xu, G.; Pusch, T.; Michalzik, R.; Hofmann, M.R.; Zutic, I.; Gerhardt, N.C. Ultrafast spin-lasers. *Nature* **2019**, *568*, 212–215. [\[CrossRef\]](#) [\[PubMed\]](#)
33. Pusch, T.; Lindemann, M.; Gerhardt, N.C.; Hofmann, M.R.; Michalzik, R. Vertical-cavity surface-emitting lasers with birefringence splitting above 250 GHz. *Electron. Lett.* **2015**, *51*, 1600–1602. [\[CrossRef\]](#)
34. Huang, Y.; Zhou, P.; Li, N. Broad tunable photonic microwave generation in an optically pumped spin-VCSEL with optical feedback stabilization. *Opt. Lett.* **2021**, *46*, 3147–3150. [\[CrossRef\]](#) [\[PubMed\]](#)
35. Torre, M.S.; Susanto, H.; Li, N.; Schires, K.; Salvade, M.F.; Henning, I.D.; Adams, M.J.; Hurtado, A. High frequency continuous birefringence-induced oscillations in spin-polarized vertical-cavity surface-emitting lasers. *Opt. Lett.* **2017**, *42*, 1628–1631. [\[CrossRef\]](#)
36. Alharthi, S.S. Broad tunable photonic microwave signal generation using optically-injected 1310 nm spin-VCSELs. *Results Phys.* **2022**, *42*, 106007. [\[CrossRef\]](#)
37. Paranthoen, C.; Levallois, C.; Brevalle, G.; Perrin, M.; Le Corre, A.; Chevalier, N.; Turban, P.; Cornet, C.; Folliot, H.; Alouini, M. Low Threshold 1550-nm Emitting QD Optically Pumped VCSEL. *IEEE Photonics Technol. Lett.* **2021**, *33*, 69–72. [\[CrossRef\]](#)
38. Alharthi, S.S.; Orchard, J.; Clarke, E.; Henning, I.D.; Adams, M.J. 1300 nm optically pumped quantum dot spin vertical external-cavity surface-emitting laser. *Appl. Phys. Lett.* **2015**, *107*, 151109. [\[CrossRef\]](#)
39. Adams, M.J.; Alexandropoulos, D. Analysis of Quantum-Dot Spin-VCSELs. *IEEE Photonics J.* **2012**, *4*, 1124–1132. [\[CrossRef\]](#)
40. Georgiou, P.; Tselios, C.; Mourkioti, G.; Skokos, C.; Alexandropoulos, D. Effect of excited state lasing on the chaotic dynamics of spin QD-VCSELs. *Nonlinear Dyn.* **2021**, *106*, 3637–3646. [\[CrossRef\]](#)
41. Li, N.; Susanto, H.; Cemlyn, B.R.; Henning, I.D.; Adams, M.J. Mapping bifurcation structure and parameter dependence in quantum dot spin-VCSELs. *Opt. Express* **2018**, *26*, 14636–14649. [\[CrossRef\]](#) [\[PubMed\]](#)
42. Qasaimeh, O. Effect of doping on the polarization characteristics of spin-injected quantum dot VCSEL. *Opt. Quantum Electron.* **2014**, *47*, 465–476. [\[CrossRef\]](#)
43. Chen, C.-Y.; Cheng, C.-H.; Lin, F.-Y. Single-sideband photonic microwave generation with an optically injected quantum-dot semiconductor laser. *Opt. Express* **2016**, *24*, 30537–30546. [\[CrossRef\]](#) [\[PubMed\]](#)

44. Jiang, Z.; Wu, Z.; Yang, W.; Hu, C.; Jin, Y.; Xiao, Z.; Xia, G. Numerical investigation on photonic microwave generation by a sole excited-state emitting quantum dot laser with optical injection and optical feedback. *Chin. Phys. B* **2021**, *30*, 050504. [[CrossRef](#)]
45. Olejniczak, L.; Panajotov, K.; Thienpont, H.; Sciamanna, M. Self-pulsations and excitability in optically injected quantum-dot lasers: Impact of the excited states and spontaneous emission noise. *Phys. Rev. A* **2010**, *82*, 023807. [[CrossRef](#)]
46. Alexandropoulos, D.; Al-Seyab, R.; Henning, I.; Adams, M. Instabilities in quantum-dot spin-VCSELs. *Opt. Lett.* **2012**, *37*, 1700–1702. [[CrossRef](#)]
47. Homayounfar, A.; Adams, M.J. Analysis of SFM dynamics in solitary and optically-injected VCSELs. *Opt. Express* **2007**, *15*, 10504–10519. [[CrossRef](#)]

Disclaimer/Publisher’s Note: The statements, opinions and data contained in all publications are solely those of the individual author(s) and contributor(s) and not of MDPI and/or the editor(s). MDPI and/or the editor(s) disclaim responsibility for any injury to people or property resulting from any ideas, methods, instructions or products referred to in the content.